JGR Solid Earth

RESEARCH ARTICLE
10.1029/2018JB016804

Earthquake Focal Mechanisms and Stress Field for the Intermediate-Depth Cauca Cluster, Colombia

Y. Chang[1,2,3], L. M. Warren[2], L. Zhu[2], and G. A. Prieto[4]

[1]Department of Earth and Space Sciences, Southern University of Science and Technology, Shenzhen, China, [2]Department of Earth and Atmospheric Sciences, Saint Louis University, Saint Louis, MO, USA, [3]Department of Geophysics, School of Geodesy and Geomatics, Wuhan University, Wuhan, China, [4]Departamento de Geociencias, Facultad de Ciencias, Universidad Nacional de Colombia-Sede Bogotá, Bogotá, Colombia

Key Points:
- Cauca cluster earthquakes have various focal mechanisms with variably oriented nodal planes inconsistent with a homogeneous stress tensor
- The average intraslab stress field has slab normal compression with in-slab extension oriented ~45° from the downdip direction
- Deviation from a typical downdip extensional stress field may result from a young slab, mantle flow push, or a concave shape of the slab

Supporting Information:
- Supporting Information S1
- Table S1

Correspondence to:
Y. Chang,
changy@sustc.edu.cn

Citation:
Chang, Y., Warren, L. M., Zhu, L., & Prieto, G. A. (2019). Earthquake focal mechanisms and stress field for the intermediate-depth Cauca cluster, Colombia. *Journal of Geophysical Research: Solid Earth*, *124*, 822–836. https://doi.org/10.1029/2018JB016804

Received 1 OCT 2018
Accepted 7 JAN 2019
Accepted article online 10 JAN 2019
Published online 25 JAN 2019

Abstract Beneath southwestern Colombia, intermediate-depth earthquakes in the Cauca cluster locate in the subducting Nazca plate and in two columns extending ~40-km into the mantle wedge above the slab. To investigate the cluster, we determine focal mechanisms for 69 small-to-moderate-sized ($2.3 \leq Ml \leq 4.7$) earthquakes in the cluster by fitting short-period body wave waveforms using the cut-and-paste method. The focal mechanisms have various faulting types and variably oriented nodal planes. We invert the focal mechanisms of the intraslab earthquakes for the intraslab stress field but cannot fit the region with a homogeneous stress tensor. We find that the principal stress axes rotate with the slab geometry, which has a concave shape and increases in dip angle from north to south. The northern region has slab normal compression and similar-magnitude maximum and intermediate principal stresses. The minimum stress axis is oriented ~41° counterclockwise from the downdip direction. In the steeper southern region, the intermediate stress axis orients in the downdip direction. Deviation from a typical downdip extensional stress field may result from a buoyant young slab, an eastward mantle flow push, and/or along-strike compression from the concave shape of the slab. This stress field would allow slip along preexisting faults of various orientations, such as the trench-perpendicular seafloor features presently observed offshore, and contribute to the apparent heterogeneity of the intraslab stress field. The mantle wedge earthquakes also have various focal mechanisms but tend to have a subvertical nodal plane that aligns with the earthquake locations.

1. Introduction

Forces acting on subducting slabs include slab pull, trench suction, plate coupling, mantle flow drag, and collisional resistance (Forsyth & Uyeda, 1975). If the slab acts as a stress guide, one of the principal stress axes will be normal to the plane of the slab and the other two principal stress axes will lie in the plane of the slab (Isacks et al., 1968). At intermediate depths (50–300 km), the extensional stress axis tends to orient in the downdip direction, indicating that slab pull is the main driving force on the slab (Isacks & Molnar, 1971). The intraslab stress field, which can be estimated from earthquake focal mechanisms, may deviate from downdip extension if additional forces have a similar magnitude as slab pull or if preexisting faults of various orientations slip (Chen et al., 2004).

Various types of focal mechanisms and nodal plane orientations are observed in the Cauca cluster of intermediate-depth earthquakes in southwestern Colombia. The Cauca cluster (3.5°N–5.5°N, 77°W–75.3°W, 50- to 200-km depth; Figure 1), which has a higher seismicity rate than the subduction zone immediately to the north or south, is associated with the Cauca segment of the subducting Nazca Plate (Pennington, 1981; Syracuse et al., 2016; Vargas & Mann, 2013). High-precision relocation of cluster earthquakes shows that the earthquakes occur both within a continuous slab and in two columns, or fingers, extending ~40 km above and normal to the slab into the mantle wedge (Chang et al., 2017). The intraslab seismic zone is 15- to 20-km thick.

In this region, the global centroid moment tensor catalog (Dziewonski et al., 1981; Ekström et al., 2012) shows strike-slip, normal, and reverse faulting earthquakes with $4.9 \leq M_W \leq 7.0$ (Figure 1). Monsalve-

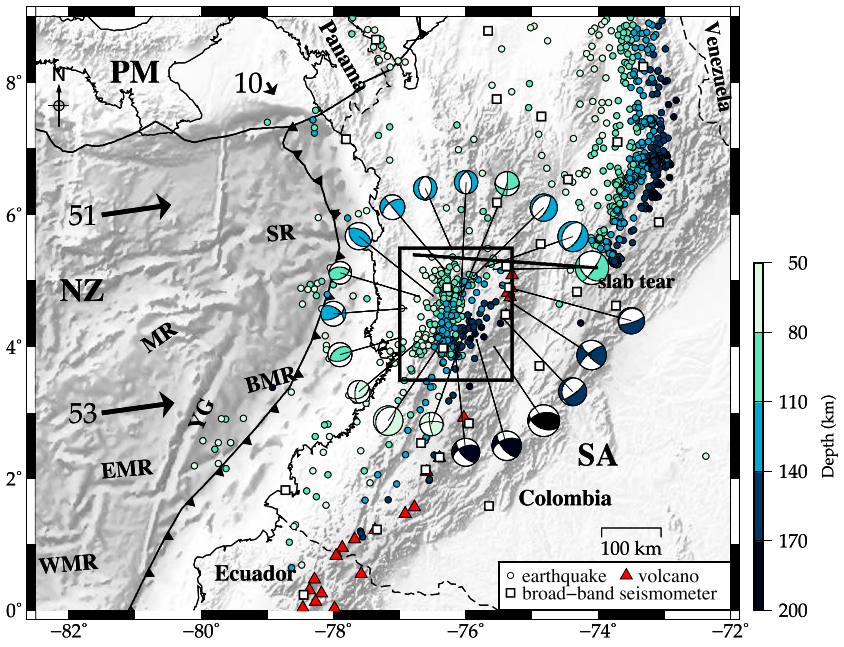

Figure 1. Study area with locations of the seismic stations (white squares and inverted triangles) and intermediate-depth earthquakes (circles shaded by depth). Beach balls show all available global centroid moment tensor solutions of intermediate-depth earthquakes (50.0 km ≤ depth ≤ 213.0 km) in the study area ranging in time from 29 May 1979 to 22 February 2015, with 4.9 ≤ Mw≤ 7.0. Black arrows with numbers indicate the velocities (mm/year) of the Nazca Plate and the Panama microplate relative to the South American Plate from model GEODVEL (Argus et al., 2010). Plate boundaries (black lines with teeth, convergent plate boundary; thick dashed lines, transform plate boundary) are from Bird (2003). Bathymetry and topography data are from ETOPO1 (Amante & Eakins, 2009). Red triangles are active volcanoes (Global Volcanism Project, 2013). Thin dashed lines are country borders. The black rectangle shows the region plotted in Figure 4. The bold black line shows the hypothesized slab tear between the Cauca segment (south of the bold black line) and Bucaramanga segment (north of the bold black line) of the subducting Nazca plate. The map labels are as follows: SR = Sandra Rift; MR = Malpelo Ridge; YG = Yaquina Graben; EMR = east Mapelo Rift; WMR = west Mapelo Rift; BMR = buried extinct rift; NZ = Nazca Plate; PM = Panama microplate; SA = South American Plate.

Jaramillo et al. (2018) also observed similarly variable focal mechanisms for four large earthquakes in the cluster. Analysis of centroid moment tensor focal mechanisms from 1976 to 2002 in combination with focal mechanisms of additional earthquakes of similar magnitudes collected by Cortés and Angelier (2005; Figure S1 in the supporting information) or alone has shown that the extensional stress axis is located in the plane of the slab, either in the downdip direction (dipping at 33° toward N98°E) (Cortés & Angelier, 2005) or rotated ~45° from the downdip direction (Chen et al., 2004). The compressional and intermediate principal stress axes have similar magnitudes (Cortés & Angelier, 2005), which may account for some of the observed focal mechanism variability.

Here we further investigate the focal mechanism variablity and dominant slab forces by determining the focal mechanisms of smaller earthquakes than previous studies and separately analyzing the intraslab and mantle wedge earthquakes. Using regional waveform data from the Servicio Geológico Colombiano (SGC), we determine the focal mechanisms of small-to-moderate-sized earthquakes (2.3 ≤ Ml ≤ 4.7) in the Cauca cluster and invert the newly obtained focal mechanisms of intraslab earthquakes for the principal stress axes. Similar to previous studies, we find various types of focal mechanisms distributed across the cluster and a stress field approximated by slab normal compression. However, the intraslab focal mechanisms are not compatible with a homogeneous stress field.

2. Study Area

The Nazca Plate is moving to the east relative to the South American Plate at a rate of ~5 cm/year (Figure 1; Lonsdale, 2005; Trenkamp et al., 2002). Subduction of the 9–15 Ma Nazca Plate is oblique to the Colombian margin (Trenkamp et al., 2002), with the strike of the trench oriented to the northeast in southern Colombia

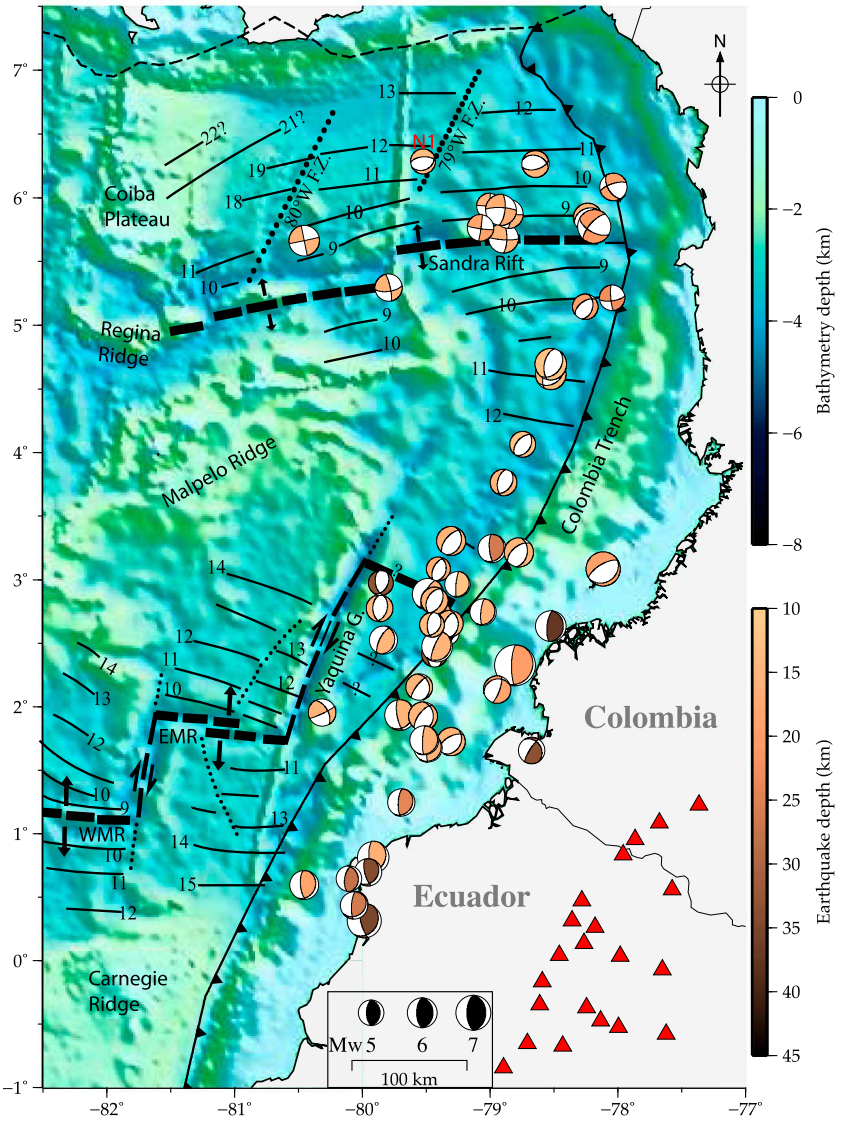

Figure 2. Global centroid moment tensor focal mechanisms of offshore earthquakes with seafloor isochron data from Lonsdale (2005). Focal mechanisms are sized by earthquake magnitude, which ranges from Mw 4.76–8.12, and color coded by depth. The focal mechanism of a mid-ocean ridge earthquake in the Panama Basin is labeled N1. Isochrons (black thin lines) are labeled with age in Ma. Rifts are plotted as black thick dashed lines with arrows showing spreading directions. Fracture zones are dotted lines. Plate boundaries (black lines with teeth, convergent plate boundary; dashed lines, transform plate boundary) are from Bird (2003). Red triangles are active volcanoes (Global Volcanism Project, 2013). The map labels are as follows: EMR = east Mapelo Rift; WMR = west Mapelo Rift; F.Z. = fracture zone; Yaquina G. = Yaquina Graben.

and rotated to the northwest north of 5.5°N (Figure 1; Argus et al., 2010). Offshore Colombia, in the outer rise, trench-parallel normal faults form and cut across the trench-perpendicular seafloor fabric, so there are both trench-parallel and trench-perpendicular preexisting weak zones in the subducting plate (Figure 2). As shown in Figure 1, the extension of the east-west oriented Sandra Rift, a spreading center active 8–13.5 Ma (Lonsdale, 2005), is collinear with an ~240-km lateral offset in intermediate-depth earthquake locations at ~5.6°N. The offset, which also appears in seismic tomography images (e.g., Chiarabba et al., 2016; Syracuse et al., 2016), suggests a tear in the subducting Nazca Plate (Vargas & Mann, 2013). The slab segments on the two sides of the slab tear have different geometries. North of the slab tear, the Bucaramanga segment extends subhorizontally to the east for 400 km before dipping at 40°–50° (Chiarabba et al., 2016; Syracuse et al., 2016). South of the slab tear, the Cauca segment (3.3°N–5.6°N)

subducts at 33°–43° without a flat segment. From ~6 to 4 Ma, the Cauca and Bucaramanga segments may have been continuous with a flat dip angle (Wagner et al., 2017). Based on the ages of igneous rocks, Wagner et al. (2017) suggest that the Cauca slab segment started to resteepen ~4 Ma, starting in the north with the slab tearing along the weak Sandra Rift.

3. Focal Mechanisms

3.1. Data and Data Preparation

From January 2010 to March 2014, the SGC catalog has 273 earthquakes in the Cauca cluster (3.5°N–5.5°N, 77.0°W–75.3°W) at depths of 50–187 km with $2.3 \leq Ml \leq 4.7$. Since the small earthquakes in the Cauca cluster typically have high signal-to-noise ratios (SNRs) within 600-km epicentral distance, we use local waveform data from 27 broadband stations (Table S1) within this distance range. Most broadband stations record 100 samples per second on the east-west, north-south, and vertical components. We extract the event waveform data from continuous seismic waveforms, correct for misoriented seismometers as identified by the SGC (Table S2), and remove the instrument response. The east-west and north-south components are rotated into the radial and transverse components.

3.2. Focal Mechanism Inversion Methodology

We use the cut-and-paste (CAP) method (Zhao & Helmberger, 1994; Zhu & Helmberger, 1996) to invert for the double-couple moment tensor from body wave waveforms. The CAP method splits the waveforms into five segments: the *P* body waves on the vertical and radial components, and the S body waves on the vertical, radial, and transverse components. The inversion procedure allows the observed *P* and *S* waveform segments to have different time shifts relative to the corresponding predicted waveforms to obtain the best waveform fit. To improve the SNRs, the waveforms are filtered in frequency bands that are individually adjusted according to the data characteristics and quality. For earthquakes with $Ml \geq 3.8$, we use a frequency band of 0.1–0.5 Hz for the P segments and 0.1–0.3 Hz for the *S* segments. For earthquakes with $2.3 \leq Ml < 3.8$, we apply frequency bands of 0.5–0.8 and 0.2–0.5 Hz to the *P* and the *S* waves, respectively. We choose maximum time window lengths for the *P* and *S* segments based on the maximum hypocentral distances of the stations to the event.

We calculate synthetic waveforms using a 1-D velocity model (Table S3) modified from the global IASPEI91 model (Kennett & Engdahl, 1991) with a 50-km-thick crust to match the average crustal thickness of the northern Andes (Poveda et al., 2015). Without using a priori knowledge of source parameters, we run a grid search over the entire ranges of strike, dip, and rake angles and a wide depth range (Table S4). The latitude and longitude, taken from Chang et al. (2017), are held constant. Because of the time shifts for *P* and *S* waveform segments, focal mechanism results of CAP are insensitive to the velocity model and are tolerant to imprecision in event location (Zhao & Helmberger, 1994). However, since the depth trades off with moment magnitude M_W and velocity model, it is not as well constrained as the focal mechanism. Thus, we prefer the depth previously computed by Chang et al. (2017) using double-difference earthquake relocation. In the double-difference method, the earthquakes are precisely located relative to one another (rather than independently) and all hypocentral parameters can vary (not just depth).

The strike, dip, and rake that minimize the difference between the observed and synthetic waveforms are identified as the focal mechanism solution. We grade the solutions based on earthquake magnitude ($Ml \geq 3.8$ or $Ml < 3.8$) and variance reduction (>40% or <40%): A (excellent) solutions have high magnitude and high variance reduction, B (very good) solutions have low magnitude and high variance reduction, C (good) solutions have high magnitude and low variance reduction, and D (fair) solutions have low magnitude and low variance reduction.

3.3. Example Focal Mechanism Inversion

As an example of the focal mechanism inversion, we present the 21 July 2013 earthquake (Mw 3.62, Ml 3.5) in Figure 3. This earthquake has a grade A solution and is event number 54 in Figure 4 and Table S5. The SGC catalog depth is 112.4 km and the relocation depth is 115.28 km, so we search over a possible depth range of 60–180 km with 5-km steps (Figure 3a). The minimum misfit solution, which has a variance reduction of 76%, is a strike-slip mechanism at a depth of 98.3 ± 2.8 km. For this solution, the predicted waveforms fit the observations well in shape and amplitude (Figures 3b and 3c). Similar focal mechanism solutions are found over a wide depth range (Figure 3a), indicating that the focal mechanism is well constrained by the data.

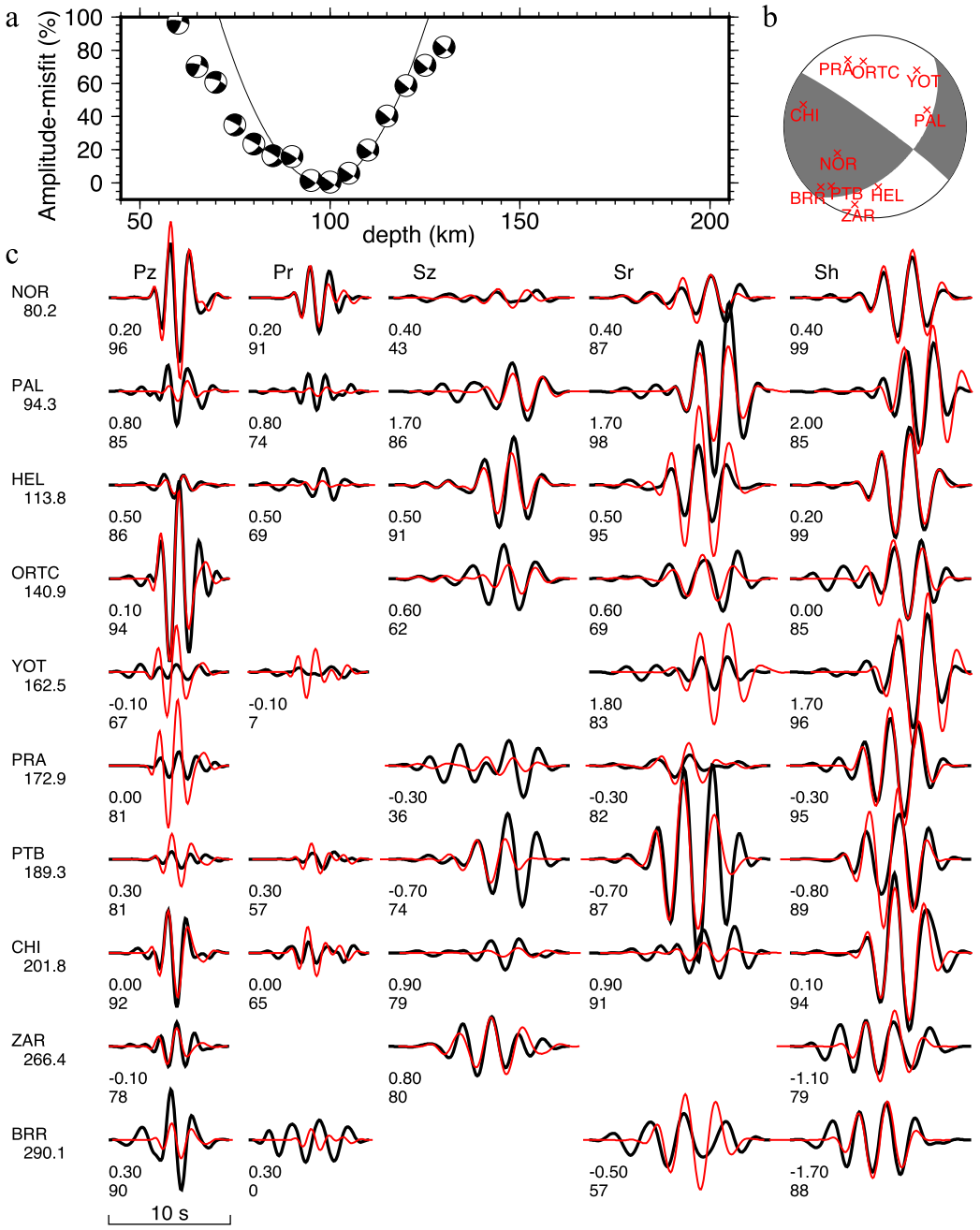

Figure 3. Focal mechanism inversion for a Ml 3.5 earthquake that occurred on 21July 2013 (event #54 in Figure 4). (a) The best focal mechanisms obtained at different focal depths. The parabola through three focal mechanisms around the minimum misfit yields the best focal depth of 98.3 ± 2.8 km. (b) The best focal mechanism with projections of station locations (xs labeled with station names) on the focal sphere. (c) Waveform fits. The station name with epicentral distance in km are listed on the left. The five waveform columns are *P* body waves on the vertical (Pz) and radial (Pr) components and *S* body waves on the vertical (Sz), radial (Sr), and transverse (Sh) components. Black and red traces represent the observed and synthetic displacement waveforms, respectively. The numbers beneath each trace segment are the time shifts in seconds and cross-correlation coefficients in percentage.

3.4. Focal Mechanism Results

Analyzing earthquakes with high SNRs at ≥6 stations, we obtain focal mechanisms of 69 small-to-moderate-sized earthquakes using CAP (Figures 4 and 5, Table S5). There are 17 earthquakes with Ml ≥3.8 and 52 earthquakes with 2.3 ≤ Ml < 3.8. Based on the precise relative locations found by Chang et al. (2017), we

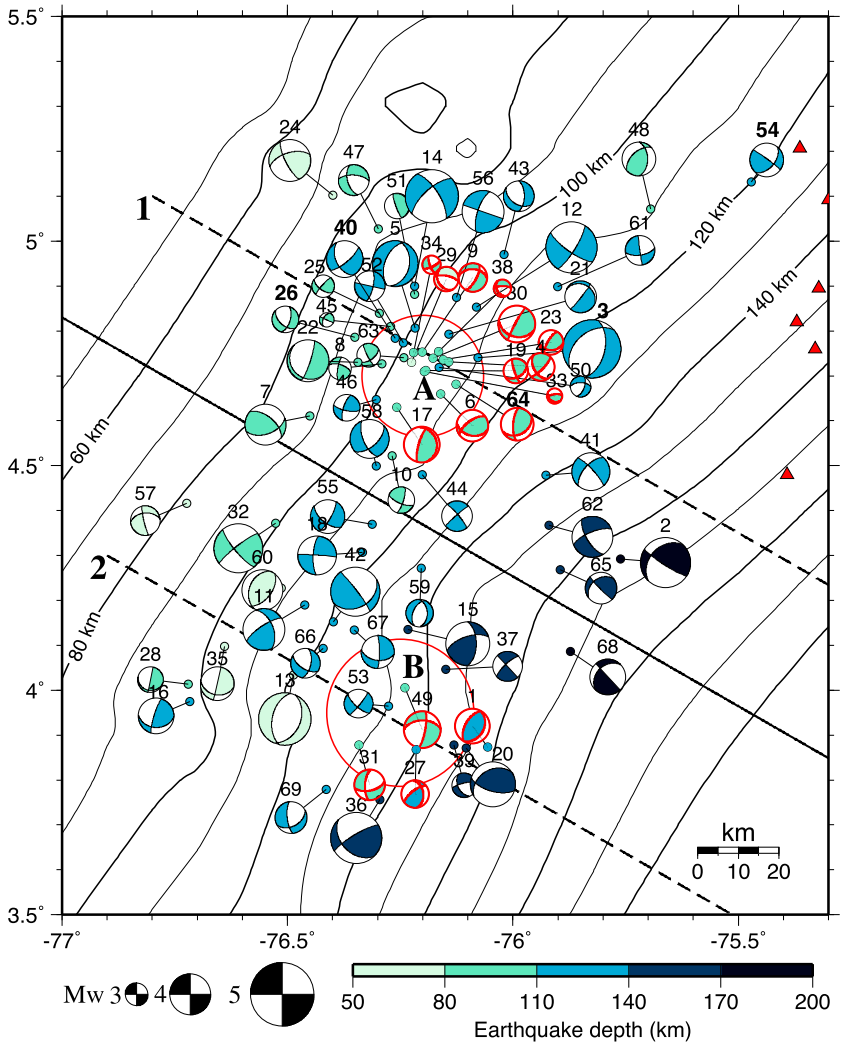

Figure 4. Cut-and-paste focal mechanisms of earthquakes in the Cauca cluster. The compressional quadrants are shaded by the relocated earthquake depth from Chang et al. (2017). The sizes of the focal spheres are scaled to the moment magnitude. The number above each focal mechanism identifies the earthquake number (Table S5); bold numbers are used for earthquakes discussed in the text. Contours (curved black lines labeled with depth) of the top surface of the intraslab seismic zone are from Chang et al. (2017). The solid black line divides the earthquakes into northern and southern sections. Dashed lines 1 and 2 mark locations of the cross-sections in Figure 5. The large red circles labeled A and B mark the locations of the mantle wedge fingers at the slab surface, and finger earthquakes are outlined in red. Red triangles are active volcanoes (Global Volcanism Project, 2013).

identify 53 intraslab earthquakes and 16 mantle wedge earthquakes. The northern finger of mantle wedge earthquakes has 12 earthquakes with $2.3 \leq Ml < 3.6$, and the southern finger has 4 earthquakes with $3.0 \leq Ml < 3.7$. The obtained focal mechanisms include all types of earthquakes and the nodal planes show various orientations. The dominant focal mechanism type for the intraslab earthquakes is strike slip, whereas the events in the northern finger are mostly reverse faulting mechanisms. Two events in the southern finger are strike slip and the other two are reverse faulting. The spatial patterns do not vary with solution grade (Figure S2).

The focal mechanism variability is also apparent in the *T* and *P* axis orientations, which are scattered in separated groups (Figures 6 and S3). In general, for the intraslab earthquakes, both the *T* and *P* axes dip at shallow angles: 83% of the plunges of the *T* axes and 83% of the plunges of the *P* axes are <45° (Table S5). The *T* and *P* axes are distributed over a wide range of azimuths, but the majority of *T* axes in the northern region lie

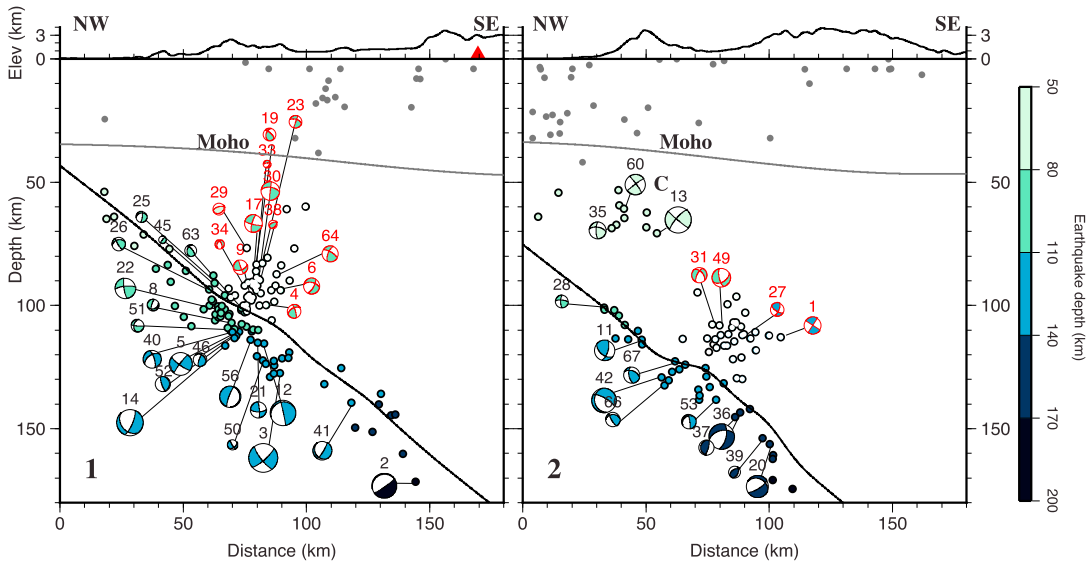

Figure 5. Northern (left; cross section 1) and southern (right; cross-section 2) cross-section views of Cauca cluster earthquakes and focal mechanisms. The cross-section locations are shown in Figure 4. Earthquakes (dots) and active volcanoes (red triangles; Global Volcanism Project, 2013) within 40 km of the profile are plotted. Intermediate-depth earthquake locations (intraslab earthquakes as colored dots, mantle wedge earthquakes as white dots) and the slab top surface model (black thick line) are from Chang et al. (2017). Unrelocated crustal earthquakes from the Servicio Geológico Colombiano catalog are plotted as gray dots. The focal mechanisms, which are shown in cross-section, are connected to the earthquake locations by black thin lines. Compressional quadrants of the focal mechanisms are shaded by the earthquake depth. The mantle wedge earthquakes are outlined in red. In the southern section, C marks the location of the three intraslab earthquakes excluded from the stress inversion. Topography is from ETOPO1 (Amante & Eakins, 2009). Moho depth is from Poveda et al. (2015).

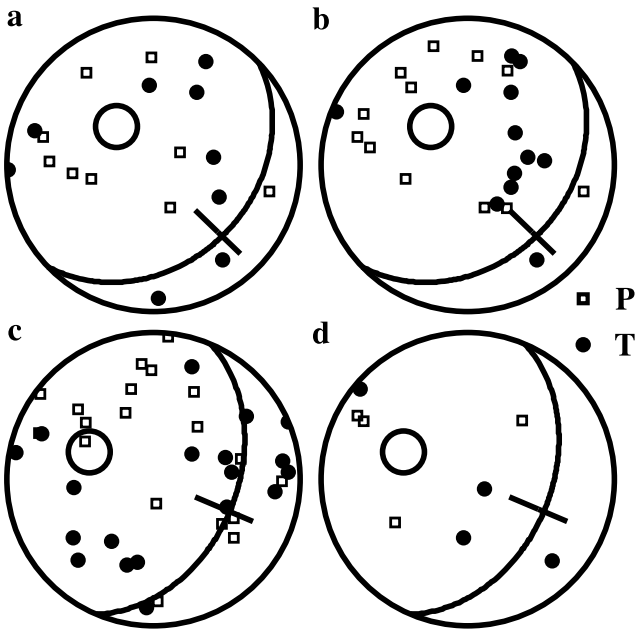

Figure 6. Lower-hemisphere projection of *T* (black dots) and *P* axes (open squares) of the focal mechanisms in (a) the northern slab segment, (b) the northern mantle wedge finger, (c) the southern slab segment, and (d) the southern mantle wedge finger. The plane of the subducting plate (heavy curve), the downdip direction (black bars), and the slab normal direction (large open circle) are shown.

in the plane of the slab (Figure 6a). In the southern region, most of the *P* axes orient in a NW-SE direction and form an acute angle with the plane of the slab, whereas the *T* axes mainly lie in a horizontal plane.

In the northern mantle wedge finger, the focal mechanisms have a consistent vertical nodal plane perpendicular to the plane of the slab and aligned with the earthquake locations (Figure 5a). The *T* and *P* axes are scattered in two separated groups (Figure 6b). The southern mantle wedge finger has too few earthquakes to identify patterns of nodal plane or *T* and *P* axis orientations (Figures 5b and 6d).

3.5. Focal Mechanism Variability

Since the focal mechanisms are so variable, we check that the different solutions are required by the waveforms. We show separate comparisons of two pairs of events, one pair with similar epicenters and similar focal mechanisms (Figures 7 and 8) and another pair with similar epicenters but contradictory focal mechanisms (Figures 9 and 10). In both pairs, the earthquakes being compared have significant differences in their waveforms. The differences could be caused by differences in the focal mechanisms, depths, magnitudes, and heterogeneous Earth structure. Since no similar earthquakes were identified during the study period (Chang et al., 2017), we cannot compare earthquakes with similar waveforms.

For the comparison of similar focal mechanisms, earthquake #26 (Ml 3.1) occurred at (4.79°N, 76.35°W, 94.33 km) on 29 December 2011 and earthquake #40 (Ml 3.8) occurred at (4.78°N, 76.26°W, 110.21 km) on 7 October 2012. The two focal mechanisms are

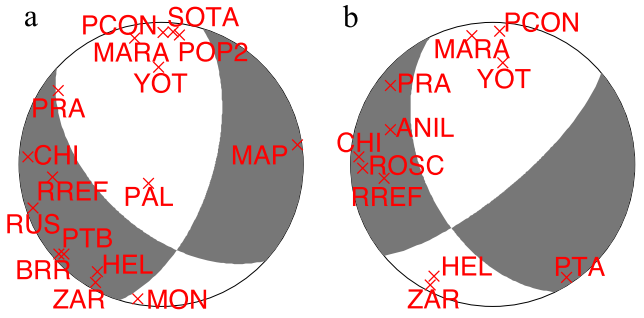

Figure 7. Lower hemisphere projections of the focal mechanisms and station locations (x labeled with station names) for (a) earthquake #26 (29 December 2011, Ml 3.1) and (b) earthquake #40 (7 October 2012, Ml 3.8).

similar but have small differences in the strike and dip of the nodal planes that can be verified by differences in the waveforms. As shown in Figure 8, the onset of the *P* wave for each event has the same polarity when the stations are in the same quadrant (such as PCON and RREF) and opposite polarity when the stations are in different quadrants (such as ZAR).

For the comparison of contradictory focal mechanisms, earthquake #3 (Ml 4.7) occurred at (4.74°N, 76.08°W, 127.37 km) on 29 January 2010 and earthquake #64 (Ml 3.2) occurred at (4.68°N, 76.13°W, 87.3 km) on 1 December 2013. While the earthquakes are separated by 40 km in depth, the similar epicenter results in similar event-to-station azimuthal angles. The two earthquakes were recorded by six common stations (Figure 10). At stations CHI, PCON, and SOTA, the waveforms show opposite directions of first motion. At station POP2, the *P* waveform of earthquake #64 is too noisy to compare. At stations HEL and PRA, earthquake #64 has more emergent *P* arrivals than earthquake #3 does. By comparing the waveforms, we confirm that the incompatible focal mechanisms are required by the data.

4. The Stress Field

4.1. Stress Inversion Methodology

Focal mechanisms can be inverted for the regional stress field if the stress field is uniform and fault planes are in different orientations. If the stress field is not homogeneous, it can be divided into smaller cells and stress tensors of each cell can be estimated using a damped regional-scale inversion method (SATSI;

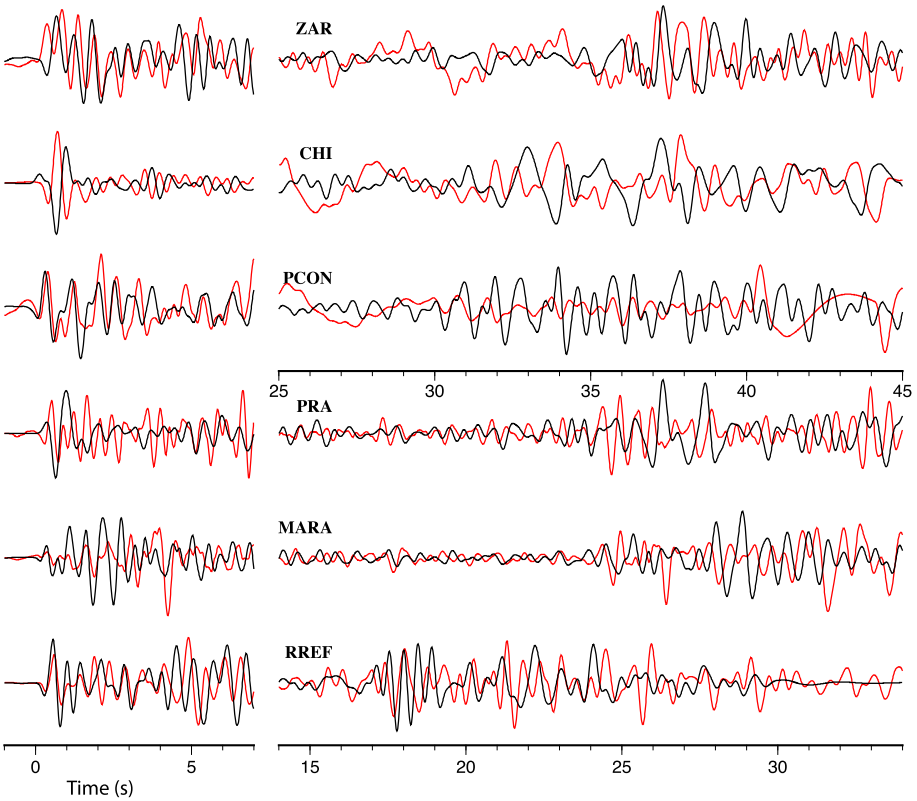

Figure 8. Waveforms of earthquakes #26 (red) and #40 (black) recorded at their common stations. The station names are given above each waveform. The waveforms are filtered between 0.5–2.0 Hz and aligned on the *P* arrivals. *P* wave segment (left) and *S* wave segment (right) are separately plotted. The amplitudes of the waveforms are normalized to have the same maximum amplitude.

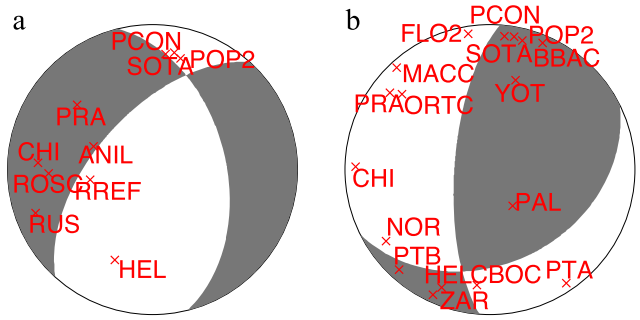

Figure 9. Lower hemisphere projections of the focal mechanisms and station locations (xs labeled with station names) for (a) earthquake #3 (29 January 2010, Ml 4.7) and (b) earthquake #64 (1 December 2013, Ml 3.2).

Hardebeck & Michael, 2006). The SATSI method obtains a stress model with minimum complexity by using an adaptive smoothing parameter that minimizes a weighted sum of the data misfit and the model length. The uncertainty of each principal stress axis orientation is estimated with 1,000 bootstrap resampling iterations. Without knowing the true fault plane, the method chooses the fault plane from the two nodal planes with equal probability. The misfit angle, defined as the angle between the slip direction and the predicted shear stress axis, quantifies the quality of the obtained stress field (Hardebeck & Michael, 2006; Michael, 1991). Small misfit angles (<45°) indicate that the focal mechanisms are consistent with the stress tensor. A low percentage (<50%) of small misfit angles means that the stress model from the inversion is inadequate to explain the data. The relative magnitude of the principal stresses ($\sigma_1 > \sigma_2 > \sigma_3$) is defined as $R = \frac{\sigma_2 - \sigma_3}{\sigma_1 - \sigma_3}$ and ranges from 0 (when $\sigma_2 = \sigma_3$) to 1 (when $\sigma_2 = \sigma_1$).

4.2. Stress Inversion: Data and Results

To separate the intraslab and mantle wedge stress fields, we sort our focal mechanisms into intraslab and mantle wedge subsets. There are too few mantle wedge earthquakes to invert for the mantle wedge stress field. To study the intraslab stress field, we start with 53 intraslab earthquakes but exclude three events (numbers 13, 35, and 60; region C on Figure 5b) that are somewhat isolated from the other intraslab events. We invert the remaining 50 focal mechanisms for one homogenous intraslab stress tensor (Figure 11a and

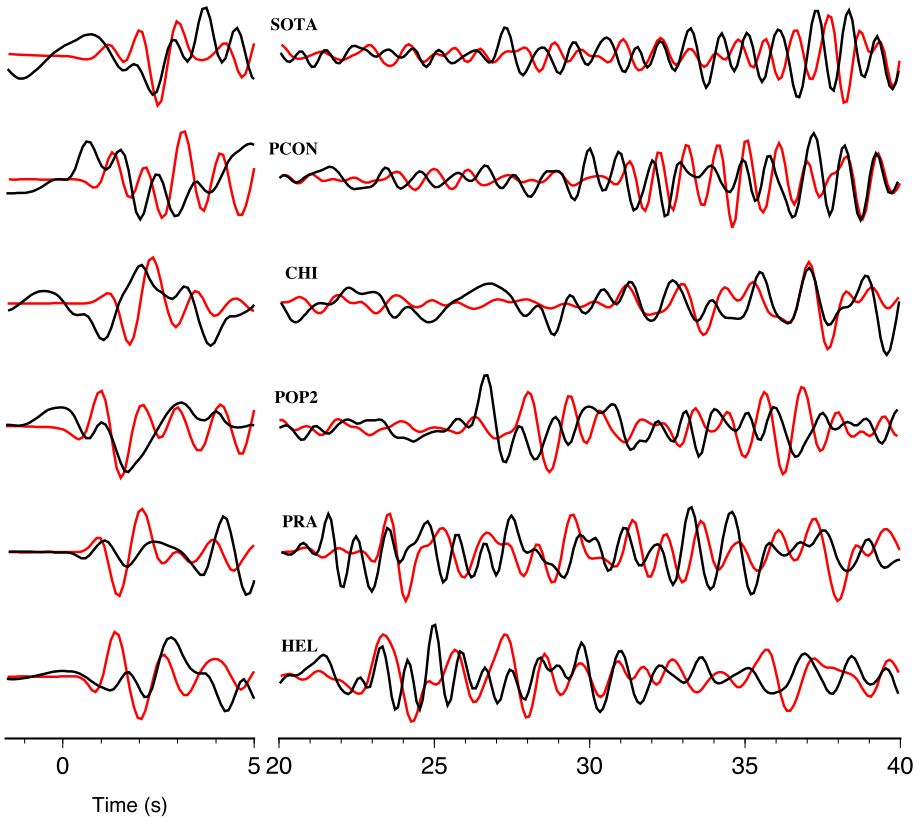

Figure 10. Waveforms of earthquakes #3 (red) and #64 (black) recorded at their common stations. The station names are given above each waveform. The waveforms are filtered between 0.2–1.0 Hz and aligned on the *P* arrivals. *P* wave segment (left) and *S* wave segment (right) are separately plotted. The amplitudes of the waveforms are normalized to have the same maximum amplitude.

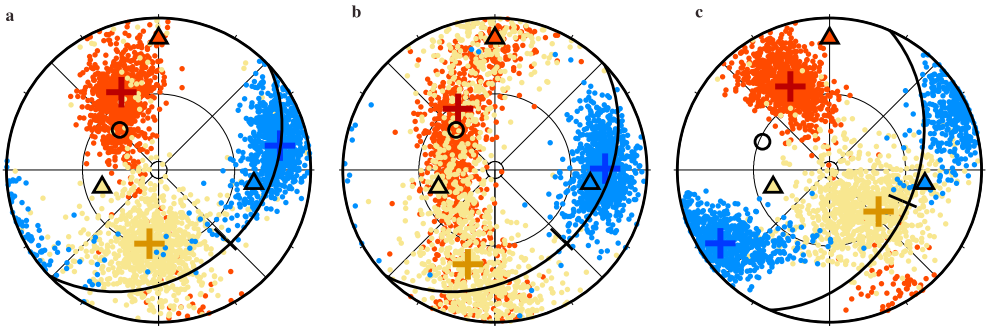

Figure 11. Lower hemisphere projection of maximum (red cross), intermediate (yellow cross), and minimum (blue cross) compressive principal stress axes of the best estimated stress tensors using (a) all Cauca segment intraslab earthquakes, (b) the northern slab earthquakes, and (c) the southern slab earthquakes. The corresponding colored dots show the uncertainty distributions from bootstrap resampling. The triangles are the principal stress axes from Cortés and Angelier (2005). The black arc in each plot represents the plane of the slab in each region, the black bar marks the downdip direction, and the black circle is the normal vector to the slab.

Table 1). This stress field has approximately slab normal compression and in-plane σ_2 and σ_3 axes. The in-slab extensional stress axis is oriented ~54° from the downdip direction of the northern section and ~39° from the downdip direction of the southern section. Even though the stress field has a tightly constrained σ_1 axis, the large average misfit angle of 67° indicates that the region is not homogeneous.

To investigate smaller, possibly homogeneous regions, we use the change in slab dip angle and direction from north to south to sort the earthquakes into northern (31 earthquakes) and southern slab sections (19 earthquakes) and estimate the stress tensors for each region with a damped inversion. We test damping parameters ranging from 0.1–2.5 and, based on the trade-off curve between the data misfit and model length (Figure S4), select a damping parameter of 1.0. As described in the rest of this section, the stress fields for the northern and southern sections (Figures 11b and 11c and Table 1) differ in orientation and relative magnitudes. In comparison with the inversion that treated the study area as one region, the damped inversion with northern and southern sections results in the same percentage (48%) of small misfit angles but a smaller average misfit angle (60° versus 67°). The earthquakes with large misfit angles (>45°) are distributed across the study area (Figure S5).

In the northern slab section (Figure 11b), the best σ_2 and σ_3 axes lie in the plane of the slab and the best σ_1 axis is normal to the plane of the slab. The σ_3 axis, which is tightly constrained by bootstrap resampling, is oriented ~41° counterclockwise from the steepest dipping direction of the slab. The σ_1 and σ_2 axes, which overlap and form a belt pattern, are close in magnitude ($R = 0.80$). The good percentage (51%) of small misfit angles and the large average misfit angle (62°) suggest that the majority of the earthquakes have nodal planes oriented in a consistent direction, but a few earthquakes have quite different fault-plane orientations and the entire region cannot be fit by a homogeneous stress tensor.

In the southern slab section (Figure 11c), the principal stress axis orientations are more distinct from one another but less aligned with the slab geometry: the best σ_1 axis is ~33° from the slab normal direction, the best σ_2 axis approximately aligns with the downdip direction of the slab, and the best σ_3 axis is subhorizontal and oriented to the southwest (neither in the plane of the slab nor normal to the slab). The average

Table 1
Results of Intraslab Stress Field Inversions

Inversion data set	Slab plane strike/dip	Number of FMs	σ_1 trend/plunge	σ_2 trend/plunge	σ_3 trend/plunge	R	SFit	AFit
All	46°/33°	50	336.5°/39.0°	194.8/44.1°	83.9°/20.2°	0.49	48%	67°
Damped, northern slab	46°/33°	31	328.9°/47.7°	195.9°/31.9°	89.3°/24.7°	0.80	51%	62°
Damped, southern slab	23°/43°	19	334.8°/35.4°	130.2°/52.0°	236.1°/12.1°	0.38	42%	56°

Note. FM = focal mechanism; σ_1 = the compressional stress axis; σ_2 = the intermediate stress axis; σ_3 = the extensional stress axis; R = the relative magnitude parameter; SFit = percentage of small (<45°) misfit angles; AFit = average misfit angle.

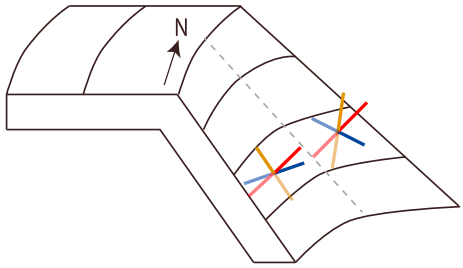

Figure 12. A schematic diagram illustrating the intraslab stress field in the Cauca segment. The gray dotted line separates the slab, which is viewed from the south, into northern and southern sections. In each section the red, yellow, and blue unit vectors represent the 3-D orientations of the maximum, intermediate, and minimum compressive principal stress axes, respectively.

misfit angle (56°) is smaller than for the northern section, but the percentage of small misfit angles (42%) is also smaller. The focal mechanisms of earthquakes in the southern section are not consistent with a single homogenous stress field.

5. Discussion

In the Cauca cluster, the 69 newly determined focal mechanisms show different faulting types and variably oriented nodal planes (Figures 4 and 5). The various, and in some cases contradictory, focal mechanisms are well constrained by the waveforms (i.e., Figure 3) and required by the differences in waveforms (i.e., Figure 10). The most common type of focal mechanism is strike slip, but all types of earthquakes are widely spread across the Cauca cluster. While variable focal mechanisms should result in tight constraints on the stress field orientation in a homogeneous region, our intraslab stress inversions show that the Cauca slab segment cannot be represented by a homogeneous stress tensor. Below, we consider the dominant forces acting on the slab and what factors, including variably oriented preexisting faults, could cause intraslab stress heterogeneity or the appearance of intraslab stress heterogeneity.

5.1. The Intraslab Stress Field

While the stress inversions indicate a heterogeneous intraslab stress field, we suggest that the resultant stress axis orientations still represent the average stress field for the region. Previously, Michael (1991) found that for a moderately varying stress field, the stress inversion returns the average stress field. The average stress regime for the entire Cauca segment, which seems to be the sum of the stress tensors in the northern and the southern sections, is slab subnormal compression with an in-slab extensional stress axis rotated ~39°–54° from the downdip direction. This neither downdip compressional nor downdip extensional orientation, which is consistent with Chen et al.'s (2004) estimation, agrees with the hypothesis of the slab acting as a stress guide (Isacks et al., 1968).

Relative to the entire Cauca segment, the northern segment has similar average principal stress orientations but more equal magnitudes of σ_1 and σ_2 whereas the southern segment has counterclockwise rotations of the σ_2 and σ_3 axes and more distinct magnitudes for the principal stress axes. The changes in the orientation of the intraslab stress field between the northern and southern sections tend to reflect the north-to-south changes in slab geometry (Figure 12). From north to south, the concave Cauca segment increases in dip angle and has a counterclockwise rotation in the dip direction. Over the same region, the intermediate stress axis rotates counterclockwise, from a shallower southward plunge to a steeper southeastward plunge in the downdip direction. The compressional and extensional stress axes have similar amounts and directions of rotation. The relative magnitude of σ_2 also changes: it is closer to σ_1 in the northern segment and closer to σ_3 in the southern segment. For the northern section, the orientation of the minimum compressional stress axis is consistent with the estimation of Cortés and Angelier (2005), but the other principal axes have a counterclockwise rotation from the estimation of Cortés and Angelier (2005).

In many subduction zones, the dominant force of slab pull results in a downdip extensional stress field (Isacks & Molnar, 1971). If slab pull were significant in the Cauca segment, we would expect downdip extension to be stronger to the south where the plate is older and further away from the free edge of the slab tear. However, we observe the opposite pattern, with the extensional stress axis oriented more horizontally in the south than in the north. The young (9–15 Ma) incoming Nazca plate (Lonsdale, 2005) may have sufficient buoyancy to reduce the effect of slab pull and allow significant contributions from other forces.

Slab pull would also be a likely mechanism to drive the slab steepening that was proposed to have begun ~4 Ma (Wagner et al., 2017). The volcanism that provides the evidence for slab steepening began at the slab tear in the north and proceeded to the south (Wagner et al., 2017), so the stronger slab pull in the north is consistent with slab steepening starting in the north.

Since slab pull does not dominate, we also consider contributions from mantle flow and the concave bend of the slab. Mantle flow beneath the Cauca segment ranges from trench-normal through the slab tear between

the Cauca and Bucaramanga segments to trench-parallel beneath the slab (Idárraga-García et al., 2016; Porritt et al., 2014). Trench-perpendicular mantle flow around the slab tear may provide a horizontal push to the slab and contribute an eastward horizontal compression to the intraslab stress field. The addition of a horizontal eastward mantle push to the southeastward slab pull could explain the northward and upward rotation of the extensional stress axis from the downdip direction in the northern section. In the southern section, the stress field orientation is less compatible with horizontal mantle flow push, suggesting that the effect of mantle flow push decreases with increasing distance from the slab tear.

The concave bend of the slab will cause along-strike compression near the top surface of the slab and along-strike extension farther below the slab surface. We expect that the earthquakes are located close to the surface of the slab and would be in a region subject to along-strike compression, with σ_1 oriented along strike in the plane of the slab. However, this orientation is incompatible with the observed slab normal σ_1 orientation.

Using our stress axis orientations and R values in combination with results from previous studies, we can make a qualitative assessment of the relative contributions of the different forces acting on the slab and how they vary over the Cauca segment. The in-plane stress axes show that the slab acts as a stress guide and that slab pull is significant, but the rotation of σ_3 from the downdip direction indicates that other forces, such as mantle push and along-strike curvature, are also important. Within the Cauca segment, shear wave splitting directions (Idárraga-García et al., 2016; Porritt et al., 2014) indicate that the magnitude of mantle flow push decreases with distance south from the slab tear. For the southern section of the Cauca segment, the rotation of the σ_1 axis in the along-strike direction of the slab suggests that along-strike compression has a larger contribution than mantle flow push.

5.2. Causes of (Apparent) Slab Heterogeneity

The contradictory focal mechanisms and the stress inversions with either large average misfit angles or small percentages of small misfit angles suggest that the intraslab stress field is not homogeneous. A heterogeneous stress tensor could result from misattribution of mantle wedge earthquakes as intraslab earthquakes or vice versa, a discontinuous slab, or heterogeneous preexisting fault orientations.

In Chang et al.'s (2017) precise earthquake locations, most of the earthquakes in the 40-km-tall mantle wedge fingers are located well above the slab and can be easily separated from the intraslab earthquakes, although it is possible that earthquakes near the intersection of the two features could be associated with the wrong feature. Indeed, several high-misfit-angle earthquakes (numbers 8, 50, 52, and 63) are located near the northern finger.

The high percentage of large misfit angles indicates that the focal mechanisms are not well fit by a homogeneous stress tensor. If the large-misfit earthquakes were concentrated in one region they could indicate a previously unmodeled structure such as a slab tear. However, their broad distribution (Figure S5), as well as the continuous 20-km-thick intraslab earthquake zone (Chang et al., 2017) and rotation of the stress tensor with the slab geometry, suggests a continuous slab in the Cauca segment.

Since the Cauca segment slab appears to be continuous, we next consider structural heterogeneities within the subducting plate. Prior to subduction, the incoming Nazca Plate has mid-ocean ridge structures and outer rise earthquakes that provide trench-perpendicular and trench-parallel preexisting weak zones. The mid-ocean ridge earthquakes, as represented by a normal earthquake in the Panama Basin (Figure 2, focal mechanism labeled N1), have approximately trench-perpendicular east-west oriented nodal planes (Figures 13a and 13d). As the slab subducts, these orientations become steeper and dip to the southeast. The outerrise earthquakes have nodal planes that strike parallel to the trench. After accounting for the angle of subduction, the nodal plane poles of outer rise earthquakes cluster at plunges of 30°–60° and trends of –45°–15° (Figures 13b and 13e). Both the rotated mid-ocean ridge and outer rise pole orientations overlap with, but are more clustered than, the observed poles for the intraslab earthquakes (Figures 13c and 13f). The overlapping orientations indicate that some of the intraslab fault orientations are consistent with the reactivation of presubduction faults, but many are not. Half of the earthquakes with large misfit angles have nodal planes consistent with the nodal planes of offshore events (Figure S6). Since preexisting faults may slip in nonoptimal orientations, they would increase the apparent heterogeneity of the intraslab stress field.

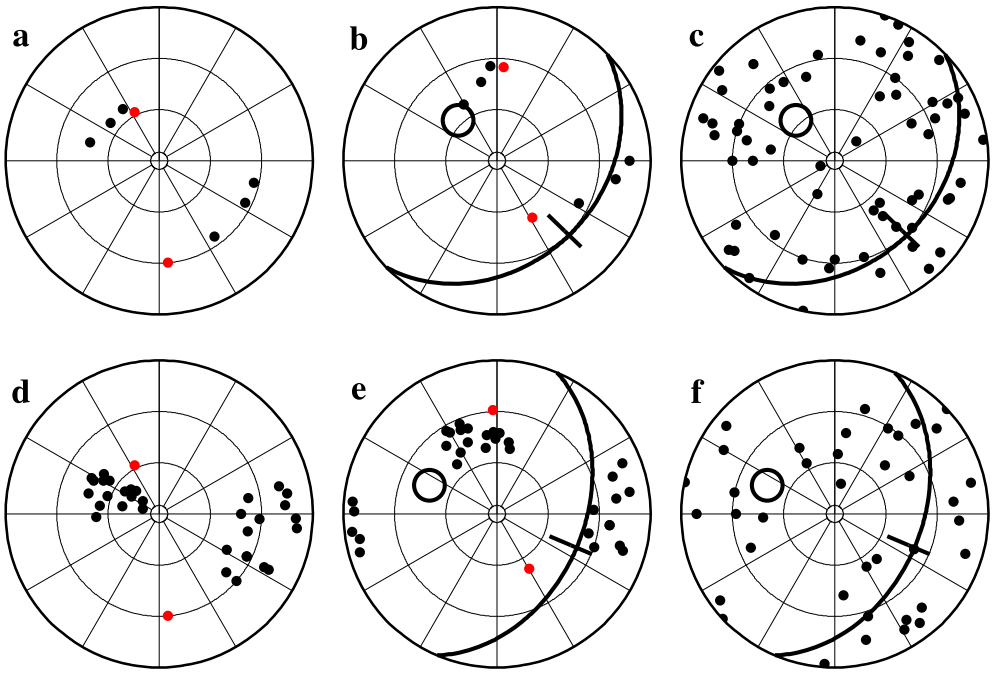

Figure 13. Lower hemisphere projection of nodal plane poles (small dots) of focal mechanisms of the outer rise, mid-ocean ridge, and intermediate-depth events for the northern (a–c) and southern (d–f) regions. For the outer rise (black dots) and mid-ocean ridge earthquakes (red dots), the poles are plotted for the actual orientation (a, d) and rotated relative to the slab geometry (b, e). (c and f) The intermediate-depth earthquakes in the slab. The plane of the subducting slab (heavy curve), the downdip direction (black bars), and the slab normal (large open circles) are plotted in (b), (c), (e), and (f).

5.3. The Mantle Wedge Earthquakes

While there are too few earthquakes in the mantle wedge to invert for the stress field, we can make some inferences about the mantle wedge earthquakes from the focal mechanisms and earthquake locations. In the northern finger, the earthquake locations are aligned with the vertical nodal plane of the focal mechanisms (Figure 5). This orientation, which is approximately perpendicular to the slab, could represent fluid propagation paths through the mantle wedge. Hydrofracture propagation direction and distance is governed by the stress field, the available volume of water, and water buoyancy (Dahm, 2000; Davies, 1999). Using realistic values for these parameters, Dahm's (2000) model of water-filled fracture propagation in the mantle wedge shows hydrofractures propagating normal to the subducting slab and extending tens of kilometers into the mantle wedge.

6. Conclusions

Earthquakes in the Cauca cluster of intermediate-depth earthquakes have a wide range of focal mechanism types and nodal plane orientations. While the focal mechanisms of the intraslab earthquakes cannot be modeled by a homogeneous stress field, we suggest that the stress inversion results represent the average intraslab stress field. The intraslab stress field rotates with the slab geometry. From north to south, the concave Cauca segment increases in dip angle and has a counterclockwise rotation in dip direction. The stress field in the northern segment has an in-slab extensional stress axis oriented 41° counterclockwise from the downdip direction and compressional and intermediate stress axes with similar magnitudes. In the southern section, the intermediate stress axis is directed in the downdip direction and the compressional and extensional stress axes are neither parallel nor perpendicular to the slab. These stress field orientations differ from the expected downdip extension that is commonly observed in slabs at intermediate depths. The atypical stress field may result from a reduction in slab pull because of the young age of the subducting Nazca plate, an increase in mantle flow push from flow through the slab tear to the north, and/or along-strike compression from the concave shape of the slab. Some of the apparent heterogeneity may also

result from some earthquakes slipping along trench-perpendicular preexisting faults. Above the slab, the mantle wedge earthquakes have locations and nodal planes consistent with the expected propagation paths of hydrofractures.

Acknowledgments
The Servicio Geológico Colombiano (SGC) earthquake catalog and event-based waveform data used in this study are available online from the SGC (https://www2.sgc.gov.co/Paginas/aplicaciones-sismos.aspx). Focal mechanisms determined in this study are provided in the supporting information to this article in Table S5. Plots were made using Generic Mapping Tools (Wessel & Smith, 1998). This study was supported by National Science Foundation grants EAR-1141905 and EAR-1760802 to L. M. W. We thank Rob Porritt and an anonymous reviewer for constructive comments that improved the manuscript.

References

Amante, C., & Eakins, B.W. (2009). ETOPO1 1 Arc-minute global relief model: Procedures, data sources and analysis, National Geophysical Data Center, NOAA, NOAA Technical Memorandum NESDIS NGDC-24.

Argus, D. F., Gordon, R. G., Heflin, M. B., Ma, C., Eanes, R. J., Willis, P., et al. (2010). The angular velocities of the plates and the velocity of Earth's centre from space geodesy. *Geophysical Journal International*, *180*(3), 913–960. https://doi.org/10.1111/J.1365-246x.2009.04463.X

Bird, P. (2003). An updated digital model of plate boundaries. *Geochemistry, Geophysics, Geosystems*, *4*(3), 1027. https://doi.org/10.1029/2001GC000252

Chang, Y., Warren, L. M., & Prieto, G. A. (2017). Precise locations for intermediate-depth earthquakes in the Cauca cluster, Colombia. *Bulletin of the Seismological Society of America*, *107*(6), 2649–2663. https://doi.org/10.1785/0120170127

Chen, P. F., Bina, C. R., & Okal, E. A. (2004). A global survey of stress orientations in subducting slabs as revealed by intermediate-depth earthquakes. *Geophysical Journal International*, *159*(2), 721–733. https://doi.org/10.1111/J.1365-246x.2004.02450.X

Chiarabba, C., De Gori, P., Faccenna, C., Speranza, F., Seccia, D., Dionicio, V., & Prieto, G. A. (2016). Subduction system and flat slab beneath the Eastern Cordillera of Colombia. *Geochemistry, Geophysics, Geosystems*, *17*, 16–27. https://doi.org/10.1002/2015GC006048

Cortés, M., & Angelier, J. (2005). Current states of stress in the northern Andes as indicated by focal mechanisms of earthquakes. *Tectonophysics*, *403*(1–4), 29–58. https://doi.org/10.1016/j.tecto.2005.03.020

Dahm, T. (2000). Numerical simulations of the propagation path and the arrest of fluid-filled fractures in the earth. *Geophysical Journal International*, *141*(3), 623–638. https://doi.org/10.1046/j.1365-246x.2000.00102.x

Davies, J. H. (1999). The role of hydraulic fractures and intermediate-depth earthquakes in generating subduction-zone magmatism. *Nature*, *398*(6723), 142–145. https://doi.org/10.1038/18202

Dziewonski, A. M., Chou, T. A., & Woodhouse, J. H. (1981). Determination of earthquake source parameters from waveform data for studies of global and regional seismicity. *Journal of Geophysical Research*, *86*(B4), 2825–2852. https://doi.org/10.1029/JB086iB04p02825

Ekström, G., Nettles, M., & Dziewoński, A. M. (2012). The global CMT project 2004–2010: Centroid-moment tensors for 13,017 earthquakes. *Physics of the Earth and Planetary Interiors*, *200-201*, 1–9. https://doi.org/10.1016/j.pepi.2012.04.002

Forsyth, D., & Uyeda, S. (1975). On the relative importance of the driving forces of plate motion. *Geophysical Journal International*, *43*(1), 163–200. https://doi.org/10.1111/j.1365-246X.1975.tb00631.x

Global Volcanism Project (2013). Volcanoes of the World, v. 4.5.0. Venzke, E (ed.). Smithsonian Institution. Downloaded 04 Jul 2016. https://doi.org/10.5479/si. GVP.VOTW4-2013

Hardebeck, J. L., & Michael, A. J. (2006). Damped regional-scale stress inversions: Methodology and examples for southern California and the Coalinga aftershock sequence. *Geophysical Journal International*, *111*, B11310. https://doi.org/10.1029/2005JB004144

Idárraga-García, J., Kendall, J. M., & Vargas, C. A. (2016). Shear wave anisotropy in northwestern South America and its link to the Caribbean and Nazca subduction geodynamics. *Geochemistry, Geophysics, Geosystems*, *17*, 3655–3673. https://doi.org/10.1002/2016GC006323

Isacks, B., & Molnar, P. (1971). Distribution of stresses in the descending lithosphere from a global survey of focal-mechanism solutions of mantle earthquakes. *Reviews of Geophysics*, *9*(1), 103–174. https://doi.org/10.1029/RG009i001p00103

Isacks, B., Oliver, J., & Sykes, L. R. (1968). Seismology and the new global tectonics. *Journal of Geophysical Research*, *73*(18), 5855–5899. https://doi.org/10.1029/JB073i018p05855

Kennett, B. L. N., & Engdahl, E. R. (1991). Traveltimes for global earthquake location and phase identification. *Geophysical Journal International*, *105*(2), 429–465. https://doi.org/10.1111/j.1365-246X.1991.tb06724.x

Lonsdale, P. (2005). Creation of the Cocos and Nazca plates by fission of the Farallon plate. *Tectonophysics*, *404*(3–4), 237–264. https://doi.org/10.1016/J.Tecto.2005.05.011

Michael, A. J. (1991). Spatial variations in stress within the 1987 Whittier Narrows, California, aftershock sequence: New techniques and results. *Journal of Geophysical Research*, *96*(B4), 6303–6319. https://doi.org/10.1029/91JB00195

Monsalve-Jaramillo, H., Valencia-Mina, W., Cano-Saldaña, L., & Vargas, C. A. (2018). Modeling subduction earthquake sources in the central-western region of Colombia using waveform inversion of body waves. *Journal of Geodynamics*, *116*, 47–61. https://doi.org/10.1016/j.jog.2018.02.005

Pennington, W. D. (1981). Subduction of the eastern Panama Basin and seismotectonics of northwestern South America. *Journal of Geophysical Research*, *86*(B11), 10,753–10,770. https://doi.org/10.1029/JB086iB11p10753

Porritt, R. W., Becker, T. W., & Monsalve, G. (2014). Seismic anisotropy and slab dynamics from SKS splitting recorded in Colombia. *Geophysical Research Letters*, *41*, 8775–8783. https://doi.org/10.1002/2014GL061958

Poveda, E., Monsalve, G., & Vargas, C. A. (2015). Receiver functions and crustal structure of the northwestern Andean region, Colombia. *Journal of Geophysical Research: Solid Earth*, *120*, 2408–2425. https://doi.org/10.1002/2014JB011304

Syracuse, E. M., Maceira, M., Prieto, G. A., Zhang, H., & Ammon, C. J. (2016). Multiple plates subducting beneath Colombia, as illuminated by seismicity and velocity from the joint inversion of seismic and gravity data. *Earth and Planetary Science Letters*, *444*, 139–149. https://doi.org/10.1016/j.epsl.2016.03.050

Trenkamp, R., Kellogg, J. N., Freymueller, J. T., & Mora, H. P. (2002). Wide plate margin deformation, southern Central America and northwestern South America, CASA GPS observations. *Journal of South American Earth Sciences*, *15*(2), 157–171. https://doi.org/10.1016/S0895-9811(02)00018-4

Vargas, C. A., & Mann, P. (2013). Tearing and breaking off of subducted slabs as the result of collision of the Panama arc-indenter with northwestern South America. *Bulletin of the Seismological Society of America*, *103*(3), 2025–2046. https://doi.org/10.1785/0120120328

Wagner, L. S., Jaramillo, J. S., Ramírez-Hoyos, L. F., Monsalve, G., Cardona, A., & Becker, T. W. (2017). Transient slab flattening beneath Colombia. *Geophysical Research Letters*, *44*, 6616–6623. https://doi.org/10.1002/2017GL073981

Wessel, P., & Smith, W. H. F. (1998). New, improved version of generic mapping tools released. *Eos, Transactions American Geophysical Union*, *79*(47), 579–579. https://doi.org/10.1029/98EO00426

Zhao, L.-S., & Helmberger, D. V. (1994). Source estimation from broadband regional seismograms. *Bulletin of the Seismological Society of America*, *84*(1), 91–104.

Zhu, L., & Helmberger, D. V. (1996). Advancement in source estimation techniques using broadband regional seismograms. *Bulletin of the Seismological Society of America*, *86*(5), 1634–1641.